Wiley Online Library
Early View publication on www.wileyonlinelibrary.com
(issue and page numbers not yet assigned;
citable using Digital Object Identifier – DOI)

J. Biophotonics 1–10 (2015) / **DOI** 10.1002/jbio.201500184

Journal of BIOPHOTONICS

FULL ARTICLE

Polarimetric assessment of healthy and radiofrequency ablated porcine myocardial tissue

Iftikhar Ahmad[*, 1, 2], *Adam Gribble*[*, 2], *Masroor Ikram*[1], *Mihaela Pop*[3], *and Alex Vitkin*[2, 4]

[1] Pakistan Institute of Engineering and Applied Science (PIEAS), Nilore 45650, Islamabad, Pakistan
[2] Division of Biophysics and Bioimaging, Ontario Cancer Institute/University Health Network and Department of Medical Biophysics, University of Toronto, 101 College Street, Toronto, Ontario M5G 1L7 Canada
[3] Sunnybrook Research Institute, Department of Medical Biophysics, University of Toronto, 2075 Bayview Avenue, Toronto, Ontario, M4N 3M5, Canada
[4] Department of Radiation Oncology, University of Toronto, 610 University Avenue, Toronto, Ontario M5G 2M9 Canada

Received 25 June 2015, revised 18 August 2015, accepted 25 August 2015
Published online 23 September 2015

Key words: radiofrequency ablation, cardiac arrhythmia, Mueller matrix polarimetry, polarization properties

Radiofrequency (RF) ablation offers a potential treatment for cardiac arrhythmia, where properly titrated energy delivered at critical sites can destroy arrhythmogenic foci. The resulting ablation lesion typically consists of a core (coagulative necrosis) surrounded by a rim of mixed viable and non-viable cells. The extent of the RF lesion is difficult to delineate with current imaging techniques. Here, we explore polarization signatures of ten *ex-vivo* samples from untreated ($n = 5$) and RF ablated porcine hearts ($n = 5$), in backscattered geometry through Mueller matrix polarimetry. Significant differences ($p < 0.01$) in depolarization, Δ_T, were observed between the healthy, RF ablated and rim regions. Linear retardance, δ, was significantly lower in the core and rim regions compared to healthy regions ($p < 0.05$). The results demonstrate a novel application of polarimetry, namely the characterization of RF ablation extent in myocardium, including the visualization of the important lesion rim region.

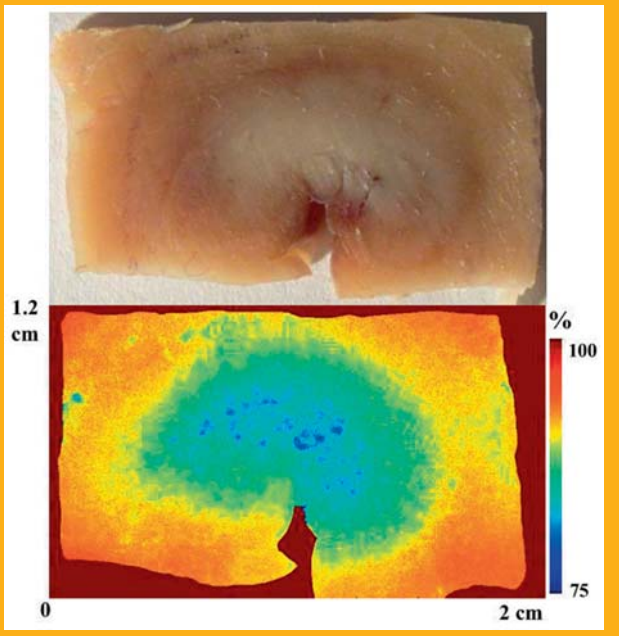

White light photo (top) of porcine myocardium tissue with radiofrequency ablation lesion and corresponding depolarization map (bottom). Depolarization is useful for visualizing the lesion core and rim.

* Corresponding authors: e-mail: iahmadmp@gmail.com, adam.gribble@mail.utoronto.ca

1. Introduction

Abnormal heart rhythms such as slow, fast or irregular heartbeats (called cardiac arrhythmias) are the leading cause of cardiovascular disease-related deaths [1]. Radiofrequency ablation (RFA) is a potential treatment for focal arrhythmia [2]. During the RFA procedure, radiofrequency (RF) energy is delivered via a catheter to specific spots to destroy arrhythmogenic regions. Accurate mapping of cardiac arrhythmias and subsequent adequate therapeutic energy delivery to the affected site(s) are the main challenges of RFA. Properly titrated RF power can control the dimensions of RFA lesion(s), conforming to the targeted volume of focal cardiac arrhythmia [3]. Typically, ablated tissue consists of a lesion core (i.e., coagulative necrotic area due to denaturation of proteins during the thermal treatment) surrounded by a rim of both viable and non-viable cells [4, 5]. The extent of the lesion and complete tissue destruction within the targeted boundaries (and consequently, RFA success) is difficult to assess with current techniques available in clinical electrophysiology. Parameters like catheter tip temperature, delivered power, heating time, and impedance change during RFA are monitored and used as indicators of lesion extent and quality assessment. However, failure to produce an RFA lesion that closely conforms to the target site and lesion contiguity remains a major setback to successful RF catheter ablation treatment of ventricular arrhythmias [6].

Medical imaging modalities such as ultrasound (US), computed tomography (CT) and magnetic resonance (MR) have their specific advantages/shortcomings for RFA guidance and post-RFA evaluation. For example, several studies have demonstrated the ability of US to monitor thermal lesions *in vitro* [7, 8]. However, the ability of this technique to accurately quantify the spatial extent of thermal damage is hindered by its relatively poor spatial resolution. CT has poor soft tissue contrast and consequently provides limited information about RFA lesion extent. The delineation of the lesion rim area with CT imaging is particularly prone to ambiguities [9]. MR is a more promising imaging modality for visualization and monitoring of the RF lesion [4]. However, it demands highly sophisticated and expensive technology with time consuming imaging algorithms. Consequently, there is a need for better and/or more affordable imaging methods to assess RFA lesion extent.

Optical imaging modalities may offer insights into microstructural characteristics of myocardial tissue and have been suggested for the assessment of RFA induced thermal damage of myocardium [10–13]. For instance, optical coherence tomography (OCT) has been shown to detect RFA lesion extent based on observed changes in birefringence and scattering coefficient [10–12]. Further, photoacoustic imaging can generate optical absorption maps based on endogenous chromophore concentrations (such as deoxy-hemoglobin [Hb]), and has been utilized for assessment of RFA lesions [13]. Polarimetry has not yet been investigated for RFA lesion assessment. However, polarized light could offer rich information content about myocardial tissue architecture and morphology, [14] which could potentially be exploited for non-invasive RFA assessment.

Polarimetric imaging offers much useful information, including measurements of depolarization, linear retardance (birefringence) and optical rotation. It has been recently investigated in a variety of biomedical fields and scenarios. For example, depolarization measurements have allowed differentiation of healthy and cancerous tissue in the colon [15, 16] and cervix [17], linear retardance measurements have been investigated for monitoring stem cell regenerative treatments in myocardium following infarct, [14] and optical rotation measurements have been used to non-invasively measure glucose levels in turbid media [18].

Cardiac tissue is a particularly suitable site for polarimetric investigations owing to the highly anisotropic nature of its constituent tissues (e.g. cardiomyocytes, collagen fibers). This anisotropy gives rise to linear retardance (closely related to the property of optical birefringence), the magnitude and direction of which can be sensitively measured with optical polarimetry. Previously, polarized light analysis of myocardial infarction, coupled with non-linear microscopy, demonstrated increased collagen content in infarct scar regions [19]. Further, structural alterations associated with myocardial infarction and treatment-induced remodeling have been studied using polarized light. This work revealed decreased linear retardance in infarcted regions due to disruption of cardiomyocyte alignment [14]. Partial recovery toward the higher healthy values was observed after stem cell regenerative treatment [14]. Collectively, these studies illustrate the capability of optical polarimetry for distinguishing between healthy and structurally altered (such as RF-ablated) regions of myocardial tissue.

In this work, we explore the capability of optical polarimetry to visualize a typical myocardial RFA lesion including the necrotic core and the rim. In particular, we investigate contrast in depolarization and linear retardance images (both magnitude and orientation) for normal and RF-ablated tissues in *ex-vivo* healthy porcine hearts, using Mueller matrix polarimetry. We hypothesize that necrosis of thermally ablated myocardial tissue leads to a loss of structural anisotropy resulting in lower linear retardance and depolarization. Such polarimetric changes may be correlated to morphological and structural changes that can be validated by histology.

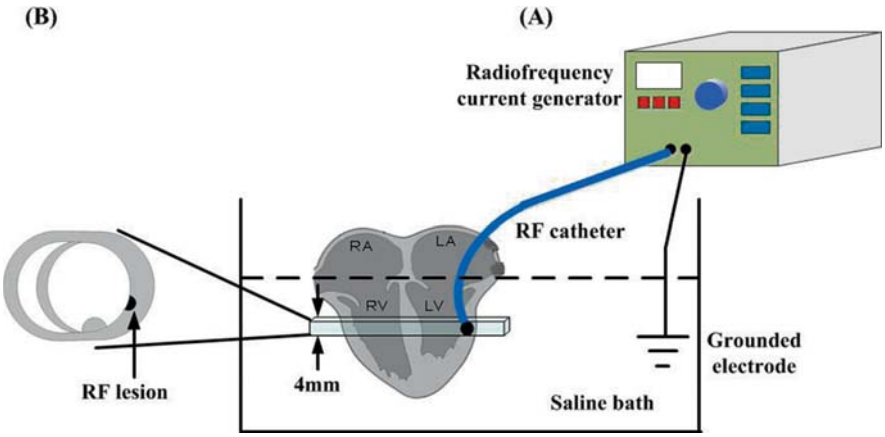

Figure 1 Schematic of (**A**) RF ablation in the porcine heart and (**B**) the resulting myocardium slice for polarimetric imaging.

2. Myocardial samples and polarimetric measurements

2.1 Sample preparation

All experiments were conducted in *ex vivo* porcine hearts. Ten heart samples (five controls, five with RFA lesions) were studied. The hearts were harvested from approximately 2-month old slaughterhouse animals weighing about 40 kg. Ablation lesions were generated inside the left ventricle (LV) via an intracardiac Navistar catheter (Biosense Webster) coupled to a 460 kHz RF generator (Radiotherapeutics, Biosense, Webster), by applying a power of 20–30 W for 40–60 sec at the tip of the catheter. The catheter was positioned onto the endocardium (either on the apex, on the septum or on the free wall of LV). Gross pathology via visual inspection confirmed the lesion formation. At the completion of the experiment, the hearts were fixed in 10% formalin for several days. After fixation, samples were cut (4 mm-thick transverse slices cut in short-axis view) and used for optical polarimetric measurements. Figure 1 shows a simplified schematic of the RF ablation set-up. Subsequently, histo-pathological evaluation was performed using Masson's trichrome staining.

2.2 Stokes–Mueller polarimetry

The polarization state of light can be completely described by a four-element vector, called a Stokes vector, $\boldsymbol{S} = [I\ Q\ U\ V]^T$. The elements I, Q, U, and V represent the total intensity, intensity difference between horizontal and linear polarization, intensity difference between linear polarization at ±45 degrees, and intensity difference between right and left circular polarization, respectively. Further, the complete set of polarization properties of the investigated sample are described by its 4×4 Mueller matrix, $\boldsymbol{M}$. In this Stokes–Mueller formalism, the interaction of a light beam of input polarization state $\boldsymbol{S}_i$

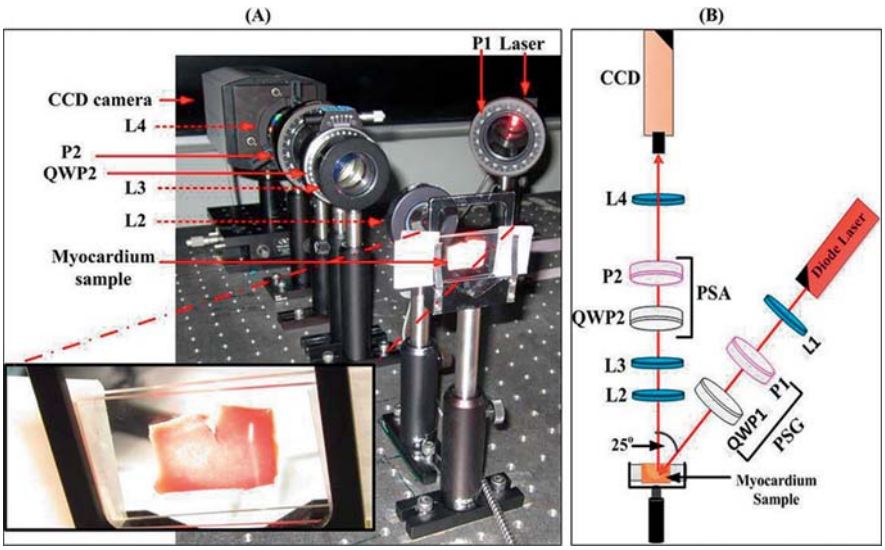

Figure 2 (**A**) White light photo of experimental Mueller matrix imaging setup. The magnified area shows an RF ablation sample illuminated in the sample holder. (**B**) Schematic of (**A**). Note that in (**A**) L1 is obstructed by P1 and that QWP1 is not present for the particular PSG configuration. PSG = polarization state generator; PSA = polarization state analyzer; P1, P2 = polarizers; QWP1, QWP2 = quarter wave plates; L1, L2, L3, L4 = lenses.

with a given sample of Mueller matrix $\boldsymbol{M}$ can be represented as

$$\boldsymbol{S}_i = \boldsymbol{M} \cdot \boldsymbol{S}_0 \tag{1}$$

where $\boldsymbol{S}_0$ is the output Stokes vector (output polarization) after interaction with the sample.

The experimentally-measured tissue Mueller matrix $\boldsymbol{M}$ is a complete description of all simultaneously occurring polarimetric processes. That is, all the polarimetric effects of the sample are reflected in the 16 elements of the Mueller matrix $\boldsymbol{M}$ in a 'lumped', complex format. For biological tissues (myocardium), the dominant polarization effects are depolarization and linear retardance (birefringence). Extraction of these individual polarimetry metrics from the all-encompassing $\boldsymbol{M}$ necessitates further decomposition of the Mueller matrix, as outlined below.

2.3 Polarimetry imaging setup

The experimental setup used for polarization measurements is illustrated in Figure 2. The myocardial tissue sample was sequentially illuminated by four different input Stokes vectors. These were generated by passing the light from a 635 nm diode laser (Thorlabs) through a polarization state generator (PSG), consisting of a polarizer P1, and quarter wave plate QWP1. The input Stokes vectors were: linear horizontal, linear vertical, linear +45°, and right circular. A wavelength of 635 nm was chosen for this experiment because it allows for greater penetration depth/sampling volume than afforded by investigations at shorter wavelengths. After interaction with the sample, the scattered light passed through the polarization state analyzer (PSA) (quarter wave plate QWP2, followed by polarizer P2) and was detected with a CCD camera (CoolSnap K4, Photometrics). Each input state was analyzed with six different output Stokes vector arrangements in the PSA optics. Specifically, the measured output states were: linear horizontal, linear vertical, linear +45°, linear –45°, right circular, and left circular. These PSG/PSA combinations resulted in 24 measurements which were used to calculate the tissue Mueller matrix $\boldsymbol{M}$, as shown in detail elsewhere [14]. All samples were analyzed in a backscattering geometry (25° off the retro-reflection direction).

2.4 Mueller matrix polar decomposition

The Mueller matrix $\boldsymbol{M}$, is the polarization transfer function of the cardiac tissues and contains the complete set of polarimetric tissue properties in its 16 elements. However, $\boldsymbol{M}$ represents the simultaneous effect of all sample polarization properties, and must be analyzed further to isolate the polarization properties of interest (i.e., depolarization, linear retardance). Mathematical decomposition of $\boldsymbol{M}$ into constituent "basis" matrices to extract these individual polarization properties is one way to "decode" the information contained in the Mueller matrix. A variety of different decompositions have been proposed and compared [20–22]. For example, comparisons between polar and differential decompositions have shown agreement in derived linear retardance (when optical rotation values are typical of biological tissues) and depolarization [20]. Taking this agreement into account, and the fact that previous polarimetry studies of the myocardium have used Lu-Chipman polar decomposition, we too use it here.

Polar decomposition is described in length elsewhere [21]. Briefly, the Mueller matrix $\boldsymbol{M}$ of the sample is expressed as the product of three component matrices, each describing a basic polarization property of the probed tissue

$$\boldsymbol{M} = \boldsymbol{M}_\Delta \cdot \boldsymbol{M}_R \cdot \boldsymbol{M}_D \tag{2}$$

where $\boldsymbol{M}_\Delta$, $\boldsymbol{M}_R$, and $\boldsymbol{M}_D$ are the component "basis" matrices associated with depolarization, retardance, and diattenuation, respectively. These effects occur simultaneously in tissue due to its turbid and heterogeneous nature, whereas each basis matrix quantifies these effects individually. Mathematical and physical consistencies and interpretations of the polar decomposition approach have been discussed at length elsewhere [21]. Here, we are particularly interested in depolarization and linear retardance, whose effects are contained in the basis matrices $\boldsymbol{M}_\Delta$ and $\boldsymbol{M}_R$ respectively.

Turbid media, such as myocardial tissue, scramble the amplitude and phase of incident photons due to extensive multiple scattering stemming from spatially heterogeneous domains of tissue properties (i.e., scatter density and refractive index), resulting in a significant reduction in polarization. The total depolarization Δ_T of the interrogated tissue can be found from the depolarization matrix $\boldsymbol{M}_\Delta$ as

$$\Delta_T = 1 - \frac{|\mathrm{tr}\,(\boldsymbol{m}_\Delta)|}{3} \tag{3}$$

where "tr" is the trace (sum of diagonal elements of a square matrix), and $\boldsymbol{m}_\Delta$ is a 3×3 sub-matrix formed by omitting the first row and column of $\boldsymbol{M}_\Delta$. Note that this quantity is related to the often-mentioned degree of polarization metric *of the state of light,* specifically DOP = $(Q^2 + U^2 + V^2)^{1/2}$/I; when comparing the value of DOP for $\boldsymbol{S}_i$ and $\boldsymbol{S}_0$, one gets

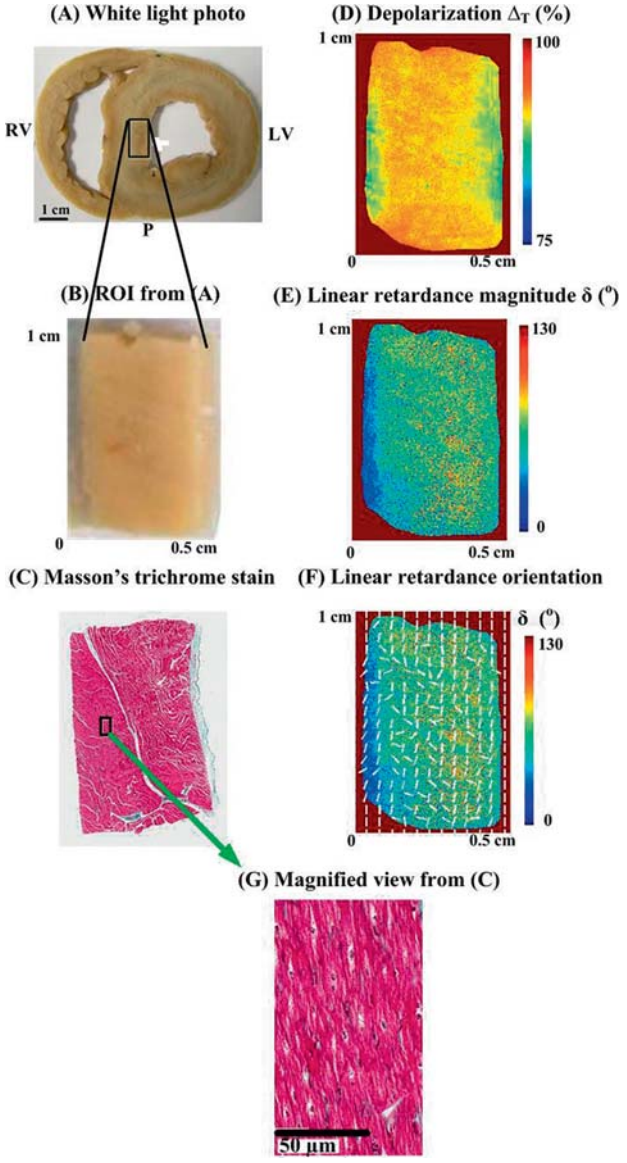

Figure 3 (**A**) White light photograph of gross untreated myocardial tissue sample (control 1) from the septum, (**B**) magnified view of ROI from the sample, (**C**) histology with Masson's trichrome staining, (**D**) depolarization map, (**E**) linear retardance magnitude map, (**F**) linear retardance orientation is represented by white dashed lines superimposed over the linear retardance magnitude map from (**E**), and (**G**) magnified (20×) histology image of healthy myocytes shown in (**C**). Scale bar = 50 µm. RV – right ventricle; LV – left ventricle; P – posterior.

some information of the depolarization properties of the interrogated tissue. In contrast, the above total depolarization Δ_T of the Mueller formalism directly yields the tissue depolarization properties without the potentially contaminating admixture of incident light polarization dependence. Overall, in many circumstances $\Delta_T \approx 1 - \mathrm{DOP}$.

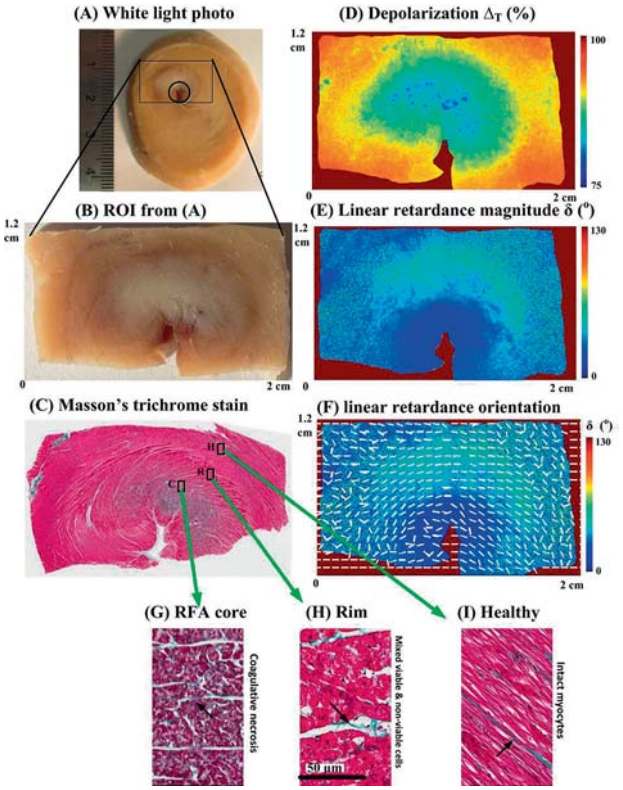

Figure 4 (**A**) White light photograph of gross myocardial tissue with RFA lesion (RFA sample 1), (**B**) magnified view of ROI from the sample, (**C**) histology with Masson's trichrome staining, (**D**) depolarization map, (**E**) linear retardance magnitude map, (**F**) linear retardance orientation is represented by white dashed lines superimposed over the linear retardance magnitude map from (**E**), and (**G–I**) magnified (20×) images of rectangular ROI boxes from RFA core, rim and healthy regions shown in (**C**), respectively. Black arrows point out collagen fibers. Scale bar = 50 µm. C – core; R – rim; H – healthy regions.

Turning to the retardance analysis, linear retardance magnitude δ of the myocardial samples was derived from the linear retardance matrix $\boldsymbol{M}_R$ by

$$\delta = \cos^{-1} \times \left[\sqrt{\{\boldsymbol{M}_R(2,2) + \boldsymbol{M}_R(3,3)\}^2 + \{\boldsymbol{M}_R(3,2) - \boldsymbol{M}_R(2,3)\}^2} - 1 \right] \quad (4)$$

where $M_R(i,j)$ are the elements of $\boldsymbol{M}_R$.

The matrix $\boldsymbol{M}_R$ is further decomposed as $\boldsymbol{M}_R = \boldsymbol{M}_{LR} \cdot \boldsymbol{M}_\varphi$ where $\boldsymbol{M}_{LR}$ and $\boldsymbol{M}_\varphi$ contain the effects of linear and circular retardance, respectively. The linear retardance orientation can be obtained from $\boldsymbol{M}_{LR}$ as

$$\theta = 0.5 \tan^{-1} \left(\frac{\boldsymbol{m}_{LR}(2,3) - \boldsymbol{m}_{LR}(3,2)}{\boldsymbol{m}_{LR}(3,1) - \boldsymbol{m}_{LR}(1,3)} \right) \quad (5)$$

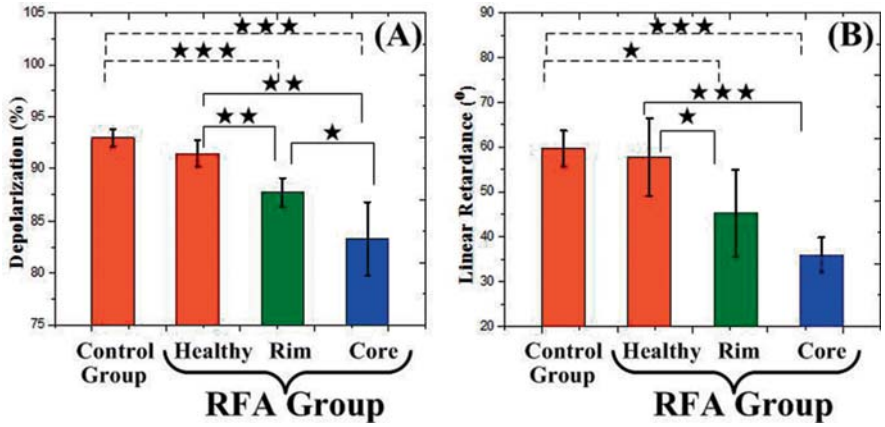

Figure 5 (**A**) Mean depolarization and (**B**) linear retardance for RFA (healthy, rim and core regions) and control samples. Error bars show standard error. * = p value < 0.05; ** < 0.01; *** < 0.001, calculated with two-tail unpaired t-test; n (RFA) = 6, n (control) = 5.

where θ is the orientation of the projection of the optical axis onto the plane perpendicular to the probing beam, and $\boldsymbol{m}_{LR}$ is a 3 × 3 sub-matrix formed by omitting the first row and column of $\boldsymbol{M}_{LR}$.

Additional details to supplement this brief description of polarimetric data analysis via polar decomposition can be found in the literature [20, 23].

3. Results

Images from two representative porcine myocardial samples are presented in Figures 3 and 4. The first sample (called control sample 1 hereafter; Figure 3A) from the septum of the myocardium served as a control (i.e., healthy myocardium with no RF ablation). A magnified view of the region analyzed with polarimetry is shown in Figure 3B.

Images showing three polarimetry metrics, depolarization, linear retardance magnitude, and linear retardance orientation, are shown in Figure 3D–F, respectively. Fairly uniform depolarization (Figure 3D) was observed throughout control sample 1. Linear retardance magnitude (Figure 3E) also appeared uniform, with slightly more variation than seen in the depolarization image. It is worth noting that both depolarization and linear retardance magnitude appear reduced at the edges of the sample. This is likely due to non-uniform thickness of the tissue (due to the cutting procedure, or to being compressed more at the edges of the sample holder); it is also possible that the photons at the edges undergoing fewer scattering events (compared to those traversing the central sample regions) is causing these reductions. To show the linear retardance orientation (Figure 3F), we superimposed dashed lines over an image of the linear retardance magnitude. These lines each represent the mean orientation directions averaged over an ROI region of 35 × 35 pixels (this ROI size was chosen for visual convenience). It is noteworthy to mention that polar Mueller matrix decomposition uses the fast optical axis as the reference axis for retardance orientation [21]. However, in cardiomyocytes it is the slow axis that is aligned with the fibers [24]. Consequently, measured retardance orientations should be shifted by 90° from the 'true' fiber directions. Indeed we found the orientation of linear retardance to be perpendicular to the myocardium fibers as viewed with histology (Figure 3C). For ease of interpretation, we have plotted the arrows in the direction of the slow optical axis, so that they reveal the myocardial fiber orientation.

The polarimetry findings were interpreted and qualitatively compared with Masson's trichrome histology, shown in Figure 3C and 3G, where the cytoplasm appears pink, nuclei are dark red, and collagen is stained blue. As revealed by histology (Figure 3G), the healthy myocardium is almost entirely composed of aligned arrays of cardiomyocytes (stained red). Occasional intervening long strands of blue stained collagen fibers were also observed.

Figure 4 shows the results from a myocardium sample with an RF lesion (RFA sample 1). The sample was from the apex of myocardium with single RFA lesion, approximately 1 cm^2 in area. The location where the RF catheter was placed in the tissue is shown by a black circle (Figure 4A). A magnified view of the region analyzed with polarimetry is shown in Figure 4B. The core of the RFA lesion appears white due to coagulative necrosis, and the perimeter is darker due to hemorrhage (red blood cells in the extravascular space due to collapsed microvessels) [5]. Depolarization, retardance magnitude, and retardance orientation images are shown in Figures 4D–F, respectively. A Masson's trichrome stain of the same sample is shown in Figure 4C and 4G–I.

Reduced depolarization values were observed in the RFA lesion compared to surrounding healthy tissue (Figure 4D). Specifically, the decrease in depolarization was more prominent at the center of RFA lesion, and increased gradually towards healthy tissue at the remote periphery of the lesion. The regions of decreased depolarization correlated well qualitatively with the spatial extent of the RFA lesion as visualized under white light and with histology. Depolarization may thus form a useful polarimetric surrogate to delineate RFA lesion extent.

The map for linear retardance magnitude (Figure 4E) demonstrates lower values for the RFA lesion compared to the healthy region. Beginning at the RFA core and progressing radially towards the healthy tissue, we observed a region of diminished linear retardance followed by a zone with moderate values and finally higher linear retardance in the healthy tissue. A corresponding gradual recovery in tissue organization (and consequently linear retardance magnitude) from RFA core towards remote healthy tissue was confirmed with histology, as described below.

In addition to linear retardance magnitude, the linear retardance orientation for RFA sample 1 is presented in Figure 4F. The linear retardance orientation is represented by white lines superimposed over the image of linear retardance magnitude. As previously mentioned, we have plotted the orientation of the slow optical axis, as this corresponds to the myocardial fiber orientation. It was observed that the retardance orientation rotates circumferentially. Closer examination of histology also revealed similar circumferential alignment of the cardiomyocytes in this treated region. Interestingly, the orientation of linear retardance is maintained in the RFA core within the ablated region. This behavior is discussed in the next section.

The optical polarimetry observations were correlated and validated with histology, shown in Figure 4C and 4G–I. In contrast to healthy tissue, as demonstrated by histology, cardiomyocytes within the RFA core region (Figure 4G) suffered thermal insult with coagulative necrosis. Cellular membrane and morphology are structurally altered but maintain some residual architecture. Nuclear integrity appears irreversibly damaged. Histological staining also showed a dark-reddish hue with black zones (due to myoglobin denaturation), which are markers of extensive thermal damage [5]. Further, close examination of collagen fibers revealed evidence of thermal damage with broken strands and random orientations. Unlike collagen in the healthy region of the myocardium, the collagen strands in the RFA lesion appear 'wavy'. The polarimetry changes due to RF ablation make sense in the context of the microstructural changes observed with histology.

For quantitative analysis, the mean depolarization and linear retardance magnitude in a region of interest (50×50 pixels) were calculated for all healthy control (Table 1) and RF treated (Table 2) samples. For RFA samples, these mean polarimetry metrics were calculated in three different regions corresponding to the RFA lesion core, lesion rim, and an undamaged healthy region. The resultant mean values are plotted in Figure 5.

Depolarization was lowest in the RFA core region and highest in the healthy regions (RFA group

Table 1 Depolarization and linear retardance magnitude of healthy control samples (ROIs = 50×50 pixels).

Control sample	Depolarization Δ_T (%)	Linear retardance magnitude δ (deg.)
1	91.6	62.1
2	93.4	58.1
3	92.7	66.2
4	94.0	55.0
5	93.1	57.0
Mean ± SD[1]	93.0 ± 0.8	59.6 ± 4.0

Table 2 Depolarization and linear retardance magnitude of samples with RFA lesions (ROIs = 50×50 pixels).

RFA sample	Depolarization Δ_T (%)			Linear retardance magnitude δ (deg.)		
	Healthy Region	Rim Region	RFA Core	Healthy Region	Rim Region	RFA Core
1	90.7	87.0	82.9	42.6	43.8	37.7
2a[2]	90.5	88.5	83.9	66.1	51.2	32.6
2b[2]	91.8	88.2	84.3	64.8	60.1	42.0
3	90.0	85.3	77.2	52.5	39.2	31.0
4	91.8	89.4	88.0	65.9	32.3	36.7
5	93.9	88.6	85.7	54.6	23.1	15.3
Mean ± SD[1]	91.5 ± 1.3	87.7 ± 1.4	83.3 ± 3.5	57.8 ± 8.7	45.3 ± 9.6	36.0 ± 3.9

[1] Standard deviation
[2] Two RFA lesions on the same sample

and control group) with intermediate values in the RFA rim region. Depolarization was significantly different between the RFA healthy, RFA rim and RFA core regions as determined by two-tailed unpaired *t*-tests ($p < 0.05$). Identical trends were seen between the control healthy, RFA rim, and RFA core regions ($p < 0.05$). There was no significant difference between the control healthy group, and the RFA healthy region, as expected.

Similarly, linear retardance magnitude was lowest in the RFA core region and highest in the healthy regions (RFA group and control group) with intermediate values in the RFA rim region. Linear retardance was significantly lower in the RFA core than the RFA healthy regions ($p < 0.05$). Identical trends were seen between the RFA core and control healthy regions ($p < 0.05$). There was no significant difference between the control healthy group and the RFA healthy region, as expected. Interestingly, although the retardance in the RFA rim region was higher than in the RFA core, the results were not significant. Based on this, depolarization may a better (more sensitive) metric for determining the extent of RFA lesions.

It is worth mentioning that the minimum depolarization and linear retardance magnitudes do not appear to be at the same location in Figure 5. This non-perfect spatial overlap is reasonable, as the two derived polarimetric parameters arise from slightly different polarized light-tissue interactions.

4. Discussion

In this study, we explored Mueller matrix polarimetry for the quantitative assessment of RFA lesions. Comparisons of depolarization and retardance maps from healthy tissue and RFA lesions demonstrated significant lesion visibility, illustrating the ability of polarimetry to detect and assess the spatial extent of RF-induced thermal damage.

The observed trends in depolarization can be interpreted by considering two factors: multiple scattering and tissue anisotropy. Multiple scattering of light is primarily due to the turbid heterogeneous nature of tissue. The amount of scattering is sensitive to tissue parameters like scatterer (cells, nuclei, connective tissue fibers, etc.) size, shape, and density, all causing complex patterns of refractive index variations. Thermal coagulation caused by high local temperatures, RF current and temperature-induced protein denaturation significantly alters normal tissue architecture including cell shape and density [26]. Overall, these alterations in tissue have been found to increase scattering [12, 26]. These effects alone would suggest increased depolarization in RFA lesions, contrary to the observed depolarization reduction.

In addition to scattering, we must consider intrinsic tissue anisotropy which also contributes towards depolarization [25, 27]. It was suggested that anisotropy contributes to increased depolarization because linear retardance magnitude and orientation may be spatially inhomogeneous, changing in various tissue micro-domains. Polarized light that passes through these micro-domains of inhomogeneous anisotropy undergoes additional randomization, and depolarization increases [28]. Based on the results of this current study, it appears that the contribution of anisotropy towards depolarization was more dominant than changes in scattering. Indeed, Alali et al. determined that myocardium muscle exhibited much higher depolarization compared to (for example) kidney cortex, despite the tissues having similar transport albedo (combination of both scattering and absorption), and suggested that anisotropy may contribute to depolarization above and beyond the effect of transport albedo [27]. Further, a decrease in linear retardance accompanied by reduced depolarization has been observed in pathological uterine cervix [17]. We posit that thermal coagulation caused by RF ablation results in loss of tissue anisotropy (supported by linear retardance findings), and a corresponding homogenization of the tissue morphology. This result in better preservation of incident light polarization, thus reduced depolarization. Although the proposed explanation of anisotropy-influenced depolarization is consistent with other studies [25, 27], we are planning additional definitive experiments for further validation. Specifically, birefringent phantoms with scattering particles will be used; by varying the amount of scatterers while keeping birefringence constant (and vice-versa), we will investigate this phenomenon further and untangle its constituent contributions.

Linear retardance (phase shift between orthogonal polarizations) arises when the refractive index of tissue is different in different spatial directions. Linear retardance is a depth-integrated measurement (as are all polarimetry metrics reported here) of the tissue's birefringent properties, and is indicative of asymmetric (aligned/anisotropic) structures. Healthy heart tissue is composed primarily of well-organized aligned cardiomyocytes, resulting in a directionally varying optical refractive index and hence strong birefringence/linear retardance. The decreased linear retardance of the RFA lesions compared to the healthy regions (Figure 4E) indicates significant disruption of this ordered striated tissue architecture due to thermal damage of cardiomyocytes, with a corresponding loss of the underlying tissue anisotropy. The gradual increase in linear retardance magnitude from RFA core to healthy regions was likely due to reduced temperature rise in areas further away from the center of lesion (RF catheter insertion point), resulting in better preservation of struc-

tural integrity/anisotropy in these regions, as confirmed by histology.

Interestingly, the orientation of linear retardance appears maintained in the RFA core. Closer examination of histology also revealed similar alignment of the damaged cardiomyocytes in the RF core region. This observed alignment may be due to a 'residual structural integrity' of myocytes, as supported by lower (but non-zero) retardance values in the RF core (Figure 4E). The thermal regime used (power and ablation time) resulted in coagulative necrosis but not in complete destruction of structural integrity. Higher power settings and longer heating times would potentially result in more severe alterations of tissue structure and complete loss of fiber orientation. However, such aggressive thermal regimes are generally avoided in clinical ablation procedures, because they can induce gas formation (popping) and emboli [29].

Although linear retardance *magnitude* is greater throughout the healthy regions of the tissue in Figure 4, these values show more spatial variation than in the RFA treated region. At the same time, the linear retardance *orientation* throughout the healthy region is also less uniform (arrows in Figure 4F appear more random/chaotic). These results would suggest that RF ablation decreases anisotropy of the myocardium (indicated by its decreased linear retardance magnitude), but over a larger scale, the residual organization becomes more consistent. This is somewhat perplexing and requires further investigation. A partial explanation may be that this is an indirect effect of the different scattering characteristics of the healthy vs. RFA tissue. Analogously, residual collagen in the RFA regions may contribute to a greater proportion to the observed linear retardance signal than it does in the healthy region. In other words, in addition to organizational changes, different biological constituents in the untreated and RF-ablated tissues may be causing the observed retardance (and depolarization) results. Finally, changes in fiber orientation with depth (axial heterogeneity) were not specifically investigated in this study. The presented polarimetry measurements are not depth-resolved per se, but rather represent cumulative polarization effects over the sampling depth (3–4 mm in most mammalian tissues) [30]. Indeed, we've begun to quantify the effects of depth heterogeneity in the context of tissue polarimetry [31].

Polarimetry was able to distinguish between healthy and RF ablated myocardium, similar to other optical techniques such as OCT [10–12] and photoacoustic imaging [13]. OCT has superior resolution (axially and laterally) in scattering media, and its polarization sensitive version (PS-OCT) is able to use polarized light to measure tissue birefringence. OCT also provides depth-resolved images thru the mechanism of coherence gating. However, it offers reduced field of view and shallower sampling/penetration depth compared to Mueller matrix polarimetry, and requires more complicated optics. Photoacoustic imaging benefits from a large penetration depth (~1 cm in the heart) [13] and depth-resolved images, but requires physical contact via acoustic coupling and again relatively complex instrumentation and signal processing. Further, photoacoustic RFA studies have been unable to demonstrate reliable measurements past 3 mm in depth (similar to sampling depth in polarimetry). Further, photoacoustic agreement with histological RFA margins could be improved, as past work showed only a 69% and 36% agreement with lesion size in the lateral and axial directions, respectively (however, the authors do speculate on ways to improve this) [13]. Finally, no PS-OCT or photoacoustic studies to date have segmented RFA tissues into the core, rim and healthy regions, but were limited to binary discrimination of RFA lesions from healthy tissue [10–13]; the clinically important 'rim region' with mixed viable and non-viable cells was not delineated/quantified. Our current study demonstrates the ability of polarimetry to reveal differences between all three important regions (core, healthy, and rim) of RFA tissue. Indeed, our future work will focus on automatic quantitative segmentation of polarimetric images into these three regions, with validation against quantitative histopathology. Potential combinations of these complimentary biophotonic approaches may also prove beneficial.

A limitation of our study was that the myocardium samples were fixed in formalin prior to polarimetric imaging. It has been observed that both linear retardance and depolarization of the myocardium increases following formalin fixation (~10% and 25% relative change, respectively) as a result probably from tissue organizational changes such as the cross-linking of proteins [32]. This did not limit our ability to see *differences* in the myocardium arising from thermal damage. And for comparison with histopathology slides, fixation is not an issue. That said, future studies should be done on fresh tissue, in preparation for clinical work.

Integration of optical polarimetry into current clinical myocardium imaging systems could potentially provide supplementary information. Specifically, our previous studies have shown that the extent/geometry of myocardial infarction can be sensitively demarcated non-invasively with optical polarimetry [33, 34]. Evaluation of RFA lesion extent, as demonstrated in this current study, would be another potential avenue for optical polarimetry of the myocardium. To enable such translation, the development of flexible fiber-based *in vivo* optical Mueller matrix probes is underway, by us and other groups [35].

5. Conclusions

This study demonstrates the potential of Mueller matrix polarimetry for assessment of cardiac RF ablation. Specifically, changes in depolarization and linear retardance (magnitude and orientation) associated with structural damage due to myocardial RF ablation were successfully measured and quantified. Decreased depolarization and linear retardance magnitude were observed in the core of the RFA lesion, with partial recovery in the rim region. Linear retardance orientation results were also quantified but were more difficult to interpret. Histology was used to investigate the underlying morphological changes caused by RFA and to help interpret the polarimetry signals. The findings suggest that the spatial extent of structural remodeling due to thermal-induced coagulative necrosis can be quantified by optical polarization maps, with potential future applications to evaluate RF lesion extent.

Acknowledgements This work was supported by IT Endowment and Telecom Fund, PIEAS, Higher Education Commission, Pakistan and Natural Sciences and Engineering Research Council of Canada (NSERC). Author 1 and Author 2 contributed equally to this work.

Author biographies Please see Supporting Information online.

References

[1] World Health Organization, Cardiovascular Diseases, <http://www.who.int/mediacentre/factsheets/fs317/en/>
[2] G. Lee, P. Sanders, and J. M. Kalman, Lancet **380**, 1509 (2012).
[3] W. G. Stevenson and E. Delacretaz, Heart **84**, 553 (2000).
[4] A. C. Lardo, E. R. McVeigh, P. Jumrussirikul, R. D. Berger, H. Calkins, J. Lima, and H. Halperin, Circulation **102**, 698 (2000).
[5] S. Thomsen, Proc. SPIE **3594**, 82–95 (1999).
[6] E. E. Girard, A. Al-Ahmad, J. Rosenberg, R. Luong, T. Moore, G. Lauritsch, J. Boese, and R. Fahrig, JACC Cardiovasc Imaging **4**, 259 (2011).
[7] J. M. Kalman, J. Jue, K. Sudhir, P. Fitzgerald, P. Yock, and M. D. Lesh, Am J Cardiol. **77**, 217 (1996).
[8] J. M. Kalman, A. P. Fitzpatrick, J. E. Olgin, M. C. Chin, R. J. Lee, M. M. Scheinman, and M. D. Lesh, Am. Heart J. **133**, 8 (1997).
[9] H. L. Fred, Tex Hear. Inst J. **31**, 345 (2004).
[10] J. F. De Boer, S. Srinivas, A. Malekafzali, Z. Chen, and J. Nelson, Opt Express **3**, 212 (1998).
[11] C. P. Fleming, H. Wang, K. J. Quan, and A. M. Rollins, J Biomed Opt. **15**, 030516 (2010).
[12] C. P. Fleming, K. J. Quan, H. Wang, G. Amit, and A. M. Rollins, Opt Express **18**, 3079 (2010).
[13] N. Dana, L. Di Biase, A. Natale, S. Emelianov, and R. Bouchard, Hear. Rhythm. **11**, 150 (2014).
[14] M. F. Wood, N. Ghosh, M. A. Wallenburg, S. H. Li, R. D. Weisel, B. C. Wilson, R. K. Li, and I. A. Vitkin, J Biomed Opt. **15**, 047009 (2010).
[15] I. Ahmad, M. Ahmad, K. Khan, S. Ashraf, S. Ahmad, and M. Ikram, J Biomed Opt. **20**, 56012 (2015).
[16] A. Pierangelo, A. Benali, M.-R. Antonelli, T. Novikova, P. Validire, B. Gayet, and A. De Martino, Opt. Express **19**, 1582 (2011).
[17] A. Pierangelo, A. Nazac, A. Benali, P. Validire, H. Cohen, T. Novikova, B. H. Ibrahim, S. Manhas, C. Fallet, R. Antonelli, and A. Martino, Opt Express **21**, 281 (2013).
[18] N. Ghosh, M. F. G. Wood, S. Li, R. D. Weisel, C. Brian, R. Li, and I. A. Vitkin, J Biophotonics. **2**, 145 (2009).
[19] M. A. Wallenburg, J. Wu, R. K. Li, and I. A. Vitkin, J Biophotonics. **4**, 297 (2011).
[20] S. Kumar, H. Purwar, R. Ossikovski, I. A. Vitkin, and N. Ghosh, J Biomed Opt. **17**, 105006 (2012).
[21] S. Y. Lu and R. A. Chipman, J. Opt. Soc. Am. A **13**, 1106 (1996).
[22] N. Ortega-Quijano and J. L. Arce-Diego, Opt. Lett. **36**, 1942 (2011).
[23] J. Chung, W. Jung, M. J. W. Hammer, P. S. Wilder, and Z. Chen, Appl Opt. **46**, 3038 (2007).
[24] C. Fan and G. Yao, Biomed Opt Express. **4**, 460 (2013).
[25] M. Oeff, J. J. Langberg, J. O. Franklin, M. C. Chin, H. Sharkey, W. Finkbeiner, J. M. Herre, and M. M. Scheinman, Am Hear. J **119**, 599 (1990).
[26] J. Swartling, S. Pålsson, P. Platonov, S. B. Olsson, and A. E. Andersson, Med Biol Eng Comput **41**, 403 (2003).
[27] S. Alali, M. Ahmad, A. Kim, N. Vurgun, M. F. Wood, and I. A. Vitkin, J Biomed Opt. **17**, 045004 (2012).
[28] S. L. Jacques, in Biomedical Photonics Handbook, Vol. 2, edited by T. Vo-Dinh (CRC Press, Boca Raton, FL, USA, 2015, Ch. 12).
[29] J. Seiler, K. C. Roberts-Thomson, J.-M. Raymond, J. Vest, E. Delacretaz, and W. G. Stevenson, Hear. Rhythm. **5**, 1411 (2008).
[30] N. Ghosh and I. A. Vitkin, J Biomed Opt. **16**, 110801 (2011).
[31] S. Alali, Y. Wang, and I. A. Vitkin, Biomed Opt Express. **3**, 3250 (2012).
[32] M. F. Wood, N. Vurgun, M. A. Wallenburg, and I. A. Vitkin, Phys Med Biol. **56**, N115 (2011).
[33] M. A. Wallenburg, M. F. G. Wood, N. Ghosh, and I. A. Vitkin, Opt. Lett. **35**, 2570 (2010).
[34] M. A. Wallenburg, M. Pop, M. F. Wood, N. Ghosh, G. A. Wright, and I. A. Vitkin, J. Innov. Opt. Health Sci. **03**, 109 (2010).
[35] S. Manhas, J. Vizet, S. Deby, J.-C. Vanel, P. Boito, M. Verdier, A. De Martino, and D. Pagnoux, Opt Express **23**, 3047 (2015).